

# Quantum interference between spectral bandwidth mismatched photons

Jan Krzyżanowski,<sup>1,\*</sup> Jerzy Szuniewicz,<sup>1</sup> Sanjay Kapoor,<sup>1</sup> Filip Sośnicki,<sup>1,2</sup> and Michał Karpiński<sup>1,†</sup>

<sup>1</sup>*Faculty of Physics, University of Warsaw, Pasteura 5, 02-093 Warszawa, Poland*

<sup>2</sup>*Integrated Quantum Optics, Institute for Photonic Quantum Systems (PhoQS), Paderborn University, Warburger Str. 100, D-33098, Paderborn, Germany*

Two-photon interference is a cornerstone of photonic quantum technologies. However, its practical implementation in promising hybrid architectures is severely constrained by the requirement of photon wavepacket indistinguishability, in particular, in terms of the photon linewidth and associated time scale. While narrowband filtering can improve interference visibility, it introduces significant photon loss – a critical limitation for applications. Here, we experimentally demonstrate an efficient approach to enable non-classical two-photon interference between spectral-bandwidth mismatched photons using an electro-optic time lens. We increase the visibility of Hong-Ou-Mandel interference between photons of 10-fold spectral bandwidth mismatch by more than 12 times, achieving non-classical two-photon interference visibility without spectral filtering. This result opens the possibility to efficiently integrate quantum systems operating at different time scales for hybrid quantum communication, teleportation, entanglement swapping, distributed sensing, and hybrid quantum computing.

Indistinguishable photons – photons identical in all degrees of freedom – are a fundamental resource for photonic quantum computing [1–6], quantum metrology [7], quantum communication [8], and in hybrid quantum networks [9]. Applications, such as long-distance entanglement distribution based on quantum repeaters [10, 11], rely on two-photon interference of photons originating in two separate photon sources. Hybrid two-photon interference is an inherently challenging task, as various sources emit photons with a wide variety of central wavelengths and spectral-temporal shapes, limiting the interference visibility [12, 13]. While in recent years tremendous progress has been made in sources of highly indistinguishable single photons realized via, e.g., nonlinear optical crystals [14, 15], or single quantum emitters [16, 17], the challenge remains as different applications require identical spectral-temporal properties of single photons. Therefore, one has to ensure that photons from different sources are spectrally and temporally matched. The central wavelength matching can be solved via quantum frequency conversion [18–23], while the spectral bandwidth matching requires a different approach.

The obvious way to improve spectral bandwidth indistinguishability of spectrally overlapping photons is the application of a spectral filter to the spectrally broader photon. This technique has been shown to improve the visibility of two-photon interference between mismatched sources, such as a heralded spontaneous parametric down conversion (SPDC) photon and a quantum dot photon [12, 13]. Its major drawback is the inherent high loss introduced by rejecting the photons that do not match the narrow filter linewidth. To address this issue, spectral shaping techniques have been developed that do not involve filtering or amplification. They utilize nonlin-

ear [24–26] or linear (electro-optic) [27–31] optical methods, applying spectral and temporal phases to modify the spectral-temporal profile of single photons. However, the indistinguishability of photons after such modifications was verified experimentally for spectral shifts only [20–23, 32]. The phase-only spectral bandwidth modification techniques, which improves spectral bandwidth indistinguishability [33, 34] have been applied to single photons and photon pairs [24–31, 35–39], but their two-photon interference has not yet been demonstrated.

In this work, we experimentally demonstrate non-classical two-photon interference of spectral-bandwidth mismatched photons after spectral bandwidth modification of one of the photons without spectral filtering. We used a spectral bandwidth converter based on an electro-

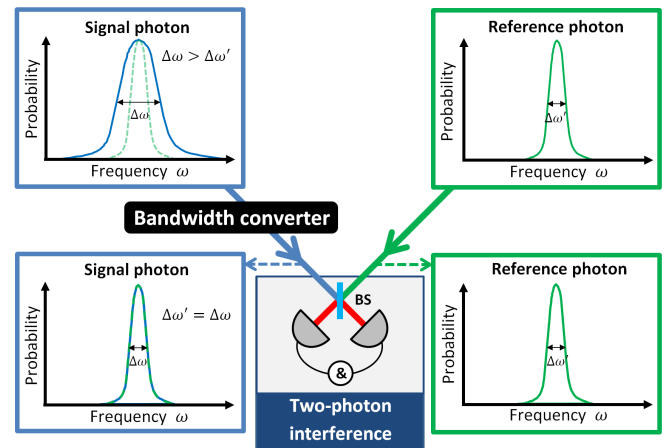


FIG. 1. Overview of the experiment. We begin with two photons with mismatched spectral bandwidths. We apply a time-lens-based spectral bandwidth converter to compress the spectrum of the signal photon to the spectral width of the reference photon. Such modification improves the overlap of the photons' spectro-temporal modes and therefore increases the indistinguishability of the photons, improving the two-photon interference visibility.

\* jan.krzyzanowski@fuw.edu.pl

† mkarp@fuw.edu.pl

optic time lens to improve the photons' indistinguishability. The converter efficiently rearranges spectral components, resulting in a narrower spectrum without spectral filtering.

The manuscript is organized as follows: first, we describe the principle of operation of the bandwidth converter, then we describe the experimental setup and the results, and at the end, we state the conclusions and provide a summary.

We present a conceptual scheme of our experiment in Fig. 1. We start with two photons with mismatched spectral bandwidths. One photon has a much broader spectrum than the other, significantly limiting their interference visibility. We apply a spectral bandwidth converter to the photon with a broader spectrum (the signal photon), compressing its spectrum to the approximate spectral width of the reference photon. We perform Hong-Ou-Mandel interference [40] between the spectrally-compressed and reference photon to observe the visibility change caused by the spectral conversion.

We use a time-lens-based bandwidth converter to match the spectral widths of interfering photons [27, 41]. We present schematically its principle of operation in Fig. 2. The spectral bandwidth compression requires manipulating the spectral and temporal phases of the light pulse. Since it features phase-only operations, in principle, it is intensity preserving.

The first stage of the bandwidth converter is the application of a quadratic spectral phase to the optical pulse, which chirps the pulse separating different spectral components linearly in time. The chirp also increases the temporal duration of the pulse. This part is experimentally realized using a dispersive medium with group delay dispersion (GDD), for example, a long single-mode fiber [27, 42].

The second stage is the time lens, which applies a quadratic temporal phase. Since a linear temporal phase implies a Doppler shift, such a quadratic phase applies a Doppler shift that changes linearly in time. Modulating a previously spectrally chirped pulse in this manner allows to target pulse's different spectral components with different spectral shifts. If the spectral ( $\Phi$ ) and temporal ( $K_{\text{eff}}$ ) quadratic phase coefficients fulfill the time lens collimation condition [41, 43]:

$$\Phi = \frac{1}{K_{\text{eff}}} \quad (1)$$

one can obtain at the output a transform limited optical pulse with a different spectral bandwidth.

To experimentally apply the temporal phase, we used a traveling wave electro-optic phase modulator (EOPM), which is based on the Pockels effect. We used a single-tone RF signal to drive the modulator, obtaining a sinusoidal phase whose extrema can be approximated by a quadratic function [44]. To achieve the best compression factor, up to the aberrations introduced by the sinusoidal phase [43], the amplitude of the quadratic phase should

satisfy the collimation condition Eq (1).

We generated photon pairs using type-II spontaneous parametric down-conversion (SPDC) in a periodically-poled potassium titanyl phosphate (PPKTP) waveguide, as shown in Fig. 3(a). The PPKTP waveguide was pumped with second harmonic (780 nm) of the output of the C-band erbium femtosecond oscillator and amplifier (Menlo Systems C-Fiber HP, 80 MHz repetition rate). The pump was spectrally filtered to 0.3 nm FWHM (full-width at half maximum) to produce degenerate photon pairs centered around 1551.5 nm. To prepare the reference photon, we applied a spectral filter using a pulse shaper (home-built) to the idler SPDC photon. We filter the reference photon's spectrum from about 2 nm FWHM to about 0.2 nm (calibrated with classical light). This implements the bandwidth mismatch between the interfering photons. Since the filter is narrower than the pump bandwidth, it also serves to remove the correlations between photons [45], effectively realizing the independent photon scenario shown in Fig. 1.

At this stage of the experiment the signal photons and reference photons exhibit different spectral bandwidths (as depicted in Fig. 3(b)). We recover their spectral compatibility by introducing the spectral bandwidth converter in the signal photon path. The bandwidth converter consists of: 1 km of thermally shielded SMF-28 fiber to introduce 22 ps<sup>2</sup> of GDD followed by a fiber-coupled lithium-niobate-waveguide EOPM (EO-Space, 16 GHz bandwidth,  $V_{\pi} = 3$  V @ 1 GHz). We drive the phase modulator using a 10 GHz sine waveform generated by an arbitrary waveform generator (AWG,

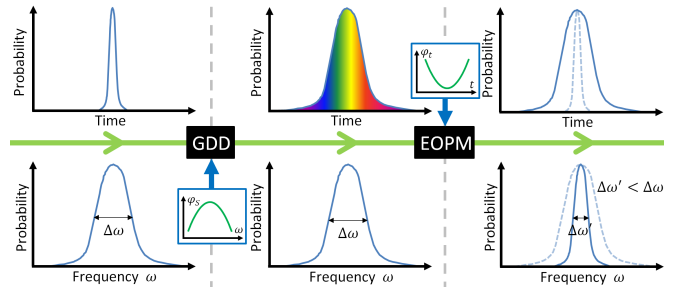


FIG. 2. The principle of operation of the spectral bandwidth converter. At the input the single-photon wavepacket is short in time and broad in spectrum (with optical frequency denoted by  $\omega$  and spectral width denoted by  $\Delta\omega$ ). The application of a quadratic phase in spectrum (denoted by  $\phi_s$ ) using the dispersive medium (exhibiting group delay dispersion, GDD) broadens photon in time and chirps it. The chirp results in arrival of different frequency components (plotted with different colors within the stretched photon's temporal envelope) at different times. The photon is then subjected to quadratic temporal phase ( $\phi_t$ ) modulation (in our experiment it is applied using an electro-optic phase modulator, EOPM). It shifts the spectral components such that they converge at the central frequency, resulting in spectral compression of the single-photon wavepacket (with spectral bandwidth denoted by  $\Delta\omega'$ ).

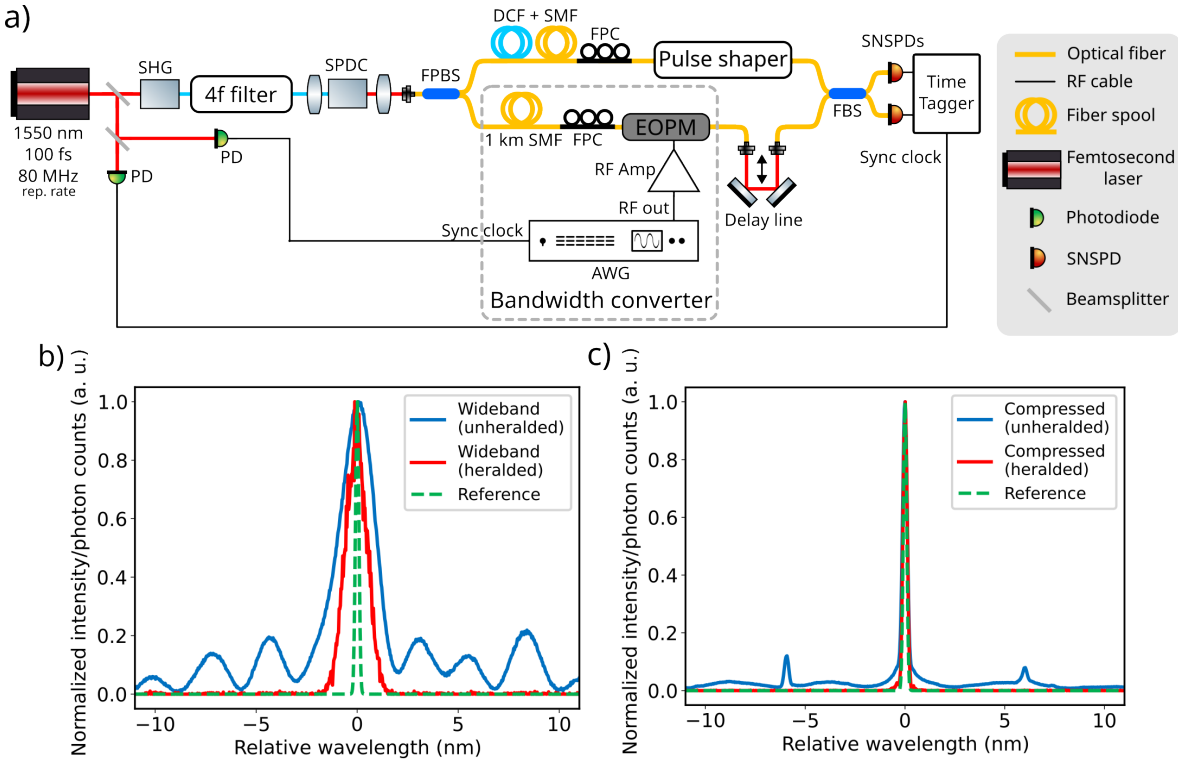


FIG. 3. Schematic of the experimental setup (a). A pair of photons is generated by the SPDC source. The reference photon is spectrally filtered using a pulse shaper. The second (unfiltered) photon is spectrally compressed using the time lens based bandwidth converter. We drive the electro-optic phase modulator (EOPM) with an RF signal from an arbitrary waveform generator (AWG) amplified by an RF amplifier. We perform two-photon interference at a 50 : 50 fiber beam splitter (FBS). In (b,c) we show the action of the time lens on the wideband photon's spectrum. The spectra from (b) are compressed by the converter resulting in the spectra, presented in (c). We show here single (blue) and coincidence counts with the narrowband photon (red) as well as classically measured transmission window of the filter as a reference. The FBS was not used for those measurements.

Keysight M8196A). We synchronized it with the laser pumping the SPDC source, which resulted in a stable delay between the RF signal and the arrival of the photon (up to residual thermal drift of the fiber length). The waveform generated by the AWG was amplified using a 3 W RF amplifier (Mini Circuits ZVE-3W-183+). We adjusted the signal amplitude at the AWG to meet the collimation condition from Eq. (1). The power transmission of the bandwidth converter is 20.6%, while the measured power transmission of the filter applied to the reference photon is only 0.6% (2.9% excluding fiber coupling losses to the filter).

We show the spectral modifications introduced by the converter in Fig. 3(b,c). The single-photon spectra are measured with a time-of-flight spectrometer utilizing the dispersive Fourier transform (DFT) technique [46]. As a dispersive medium, we used 19.8 km (336.6 ps/nm) of the SMF-28 fiber, which gives the spectral resolution of 0.22 nm for our low timing jitter detectors (11 ps RMS) [47]. The photons were detected by superconducting nanowire single photon detectors (SNSPD, Single Quantum EOS) and time tagged with a time-to-digital converter (Swabian Instruments Time Tagger Ultra). We

measured the heralded and unheralded signal photon's spectrum. We adjusted the delay between the RF signal and photon arrival to achieve the narrowest spectral width for the Fig. 3(c). This optimization ensures that the center of the chirped photon meets the cusp of the sinusoidal phase, realizing a quadratic phase. The reference spectrum in both figures is the transmission of the spectral filter measured with classical light, using an optical spectrum analyzer (OSA, Yokogawa AQ6370D).

By applying the bandwidth converter we regain matching of signal and reference photons' spectral FWHMs. However, the compressed spectrum is wider than the reference one, mainly due to the insufficient resolution of the DFT measurement. We repeated the spectral compression with classical bright light and similar parameters as in the single-photon case. We verified that the FWHM of the compressed spectrum was equal to the spectral filter bandwidth within 0.01 nm. Also, some side peaks are present in the unheralded measurements in Fig. 3 (b) arising from the non-apodized phase-matching in the PP-KTP crystal. They are not present in the heralded spectra because of the narrowband filtering of the reference photon.

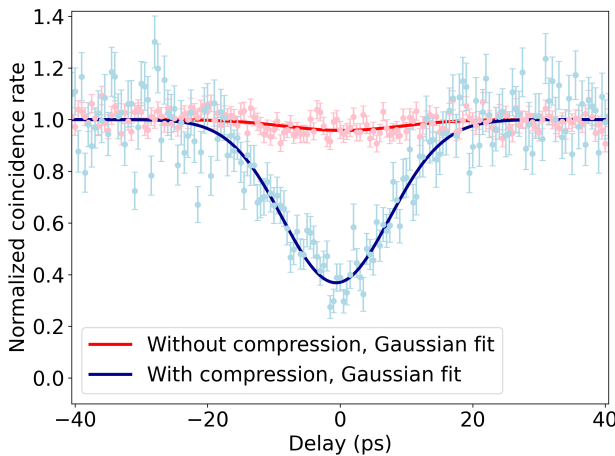


FIG. 4. Hong-Ou-Mandel interference between bandwidth mismatched photons: normalized coincidence rates between two beam splitter outputs as a function of delay between interfering photons, set at the delay line. In blue the Hong-Ou-Mandel dip after compressing the signal photon, in red the dip without the bandwidth converter. Error bars assume Poisson photon count statistics. We normalized the number of coincidences by the number of singles in both cases to remove residual photon count drifts. The low visibility dip is especially fragile for such drifts. We calculate the two-photon interference visibility from Gaussian functions (plotted with solid lines) fitted to the data. The zero point at the delay axis is calibrated to the dip position (blue data), and the position of the dip (Fig. S5(b)) observed without the spectral filter (red data).

We introduced 1 km of fiber in the path of the reference photon to compensate for the temporal delay imposed by the time lensing setup. It comprises two segments: 116 m of DCF (dispersion compensating fiber) and 948 m of SMF-28. This combination of fibers gives less than  $-0.5 \text{ ps}^2$  GDD on the delay path, which negligibly affects the spectral phase of the reference photon.

After matching the bandwidths of the photons, we performed the Hong-Ou-Mandel (HOM) interference measurement. We interfere the compressed signal and reference photons in a fiber-based 50:50 beam splitter and detect the coincidences between the photons at the FBS outputs via SNSPDs followed by a time-tagger. We applied a coincidence window of 2 ns, which is shorter than the inverse of the repetition rate of the source (12.5 ns) but much longer than the duration of the photons (about 18 ps). We used a fiber-coupled free-space delay line to control the relative delay between the photons. We measured the coincidence counts at each delay for 10 s with step of 0.5 ps. We normalized the number of coincidences by the number of singles to remove residual photon count drifts. We present the raw coincidence counts in the Supplementary Information in section S3.

The resulting HOM dip is shown in Fig. 4 in blue. We fitted a Gaussian function (with dip width, position on delay axis, multiplicative and additive constants as

fitting parameters without any constraints) to the normalized coincidence counts, which resulted in a visibility of  $(63.2 \pm 1.9)\%$ , exceeding the non-classical threshold of 50% [48]. We used the bootstrap method to estimate the visibility uncertainty assuming Poissonian photon count statistics [49].

We attribute the non-perfect interference visibility primarily to the use of non-optimal dispersion in our experimental setup. Due to limited options for dispersion compensation modules available in the laboratory, we utilized a GDD of  $\Phi = 22 \text{ ps}^2$  instead of the optimal  $\Phi \approx 11.3 \text{ ps}^2$ . Numerical simulations of this specific configuration, where the modulation amplitude was optimized to  $A = 4.3\pi \text{ rad}$ , confirm that the visibility is theoretically limited to 63.78%.

This limitation arises because operating with non-optimal dispersion exacerbates the effect of higher-order temporal aberrations inherent to the sinusoidal phase modulation, resulting in pronounced spectral side-lobes that introduce distinguishability.

Simulations indicate that with the optimal dispersion, a visibility exceeding 87% would be achievable under realistic phase modulation amplitude constraints. Visibility of 98% can be achieved with an optimal dispersion and order of magnitude higher modulation amplitude. The imperfections described above can be compensated by using a parabolic phase modulation and its proper pre-compensation due to electronics' spectral response [50] (temporal aberrations) and using a chirped fiber Bragg grating for GDD application (it would be much shorter than the used fiber, which would prevent the central wavelength drift). Details of these simulations along with analytical calculations are presented in the Supplementary Information.

To show the advantage of our bandwidth conversion scheme we removed the bandwidth converter and the reference photon's fiber delay from the setup and measured the HOM dip shown in Fig. 4 in red. For such highly mismatched photons with the spectra presented in Fig. 3(b), almost no dip is visible. We fitted a Gaussian function to the measured normalized coincidence counts, which resulted in a visibility of  $(4.2 \pm 1.9)\%$ . The coincidence counts do not form a clearly visible dip in this case. We verified that the position of the delay line is correct by observing a HOM dip without filtering the reference photon in the source (see Supplementary Information).

We further estimated the advantage of spectral compression in a practical scenario of the realization of quantum teleportation [51] using HOM interference with a bandwidth converter as a Bell-state measurement (BSM). In such experiments, the success rate of quantum teleportation is directly proportional to the HOM interference visibility [51, 52]. To calculate the final rate of correctly teleported states the HOM visibility needs to be multiplied by the transmission of the bandwidth converter (20.6%). As a reference, we considered a perfect BSM and usage of the same spectral filter as in our experi-

ment with transmission of 2.9% (already excluding fiber coupling losses – best case scenario). We obtained approximately 4.5 times improvement in the rate of correctly teleported states using the bandwidth converter, including its insertion loss.

In summary, we observed non-classical two-photon interference of photons with mismatched spectral bandwidths. Our experimental results show that introducing a time-lens-based spectral bandwidth converter improves the interference visibility from almost no visibility,  $(4.2 \pm 1.9)\%$ , to  $(63.2 \pm 1.9)\%$ , which is above the non-classical threshold of 50% [48]. It outperforms the standard filtering scheme due to higher transmission, which is limited by insertion loss only, which is expected to improve further [53, 54]. In addition, the development of low half-wave voltage EOPMs [55] is expected to reduce the effects of temporal aberrations, further improving the performance of the scheme.

The measured non-classical visibility makes the presented technique promising for quantum communication protocols such as entanglement swapping [56] or quantum teleportation [51]. The presented solution offers efficient integration of spectrally mismatched quantum systems, making a step towards building hybrid quantum repeaters [57], a vast hybrid quantum network [10] or realizing distributed quantum computing [9] in a hybrid system. It opens new perspectives in photonic quantum computing by using novel photon sources as ancilla photons for heralded nonlinearities. One of the most promising examples is matching single photons produced via quantum dots to SPDC generated photon pairs, which currently can perform two-photon interference only with high-loss narrowband filtering [12, 13]. The time lensing technique presented in this work offers much higher power transmission than the filtering in that case, which directly converts to the success rate of the quantum communication protocols beyond quantum key distribution, distributed quantum computing and sensing.

This work was supported in part by the First TEAM programme of the Foundation for Polish Science (project no. POIR.04.04.00-00-5E00/18), co-financed by the European Union under the European Regional Development Fund and in parts by the National Science Centre (Poland) under the OPUS call within the Weave programme, project no. 2023/51/I/ST7/03068 and under project no. 2022/45/N/ST2/04249, JS also acknowledges the support of START scholarship by the Foundation for Polish Science (FNP).

Rev. Lett. **99**, 250505 (2007).

- [4] A. Politi, J. C. F. Matthews, and J. L. O'Brien, Science **325**, 1221 (2009).
- [5] H.-H. Lu, J. M. Lukens, N. A. Peters, B. P. Williams, A. M. Weiner, and P. Lougovski, Optica **5**, 1455 (2018).
- [6] H. Wang, Y. He, Y.-H. Li, Z.-E. Su, B. Li, H.-L. Huang, X. Ding, M.-C. Chen, C. Liu, J. Qin, J.-P. Li, Y.-M. He, C. Schneider, M. Kamp, C.-Z. Peng, S. Hofting, C.-Y. Lu, and J.-W. Pan, Nature Photonics **11**, 361 (2017).
- [7] R. Silvestri, H. Yu, T. Stroemberg, C. Hilweg, R. W. Peterson, and P. Walther, Science Advances **10**, 0215 (2024).
- [8] H.-K. Lo, M. Curty, and B. Qi, Phys. Rev. Lett. **108**, 130503 (2012).
- [9] D. Main, P. Drmota, D. Nadlinger, E. Ainley, A. Agrawal, B. Nichol, R. Srinivas, G. Araneda, and D. Lucas, Nature, **1** (2025).
- [10] L.-M. Duan, M. D. Lukin, J. I. Cirac, and P. Zoller, Nature **414**, 413 (2001).
- [11] N. Sangouard, C. Simon, H. de Riedmatten, and N. Gisin, Rev. Mod. Phys. **83**, 33 (2011).
- [12] T. Huber, M. Prilmüller, M. Sehner, G. S. Solomon, A. Pređojević, and G. Weihs, Quantum Science and Technology **2**, 034016 (2017).
- [13] S. V. Polyakov, A. Muller, E. B. Flagg, A. Ling, N. Bormjeascaia, E. Van Keuren, A. Migdall, and G. S. Solomon, Phys. Rev. Lett. **107**, 157402 (2011).
- [14] F. Graffitti, P. Barrow, M. Proietti, D. Kundys, and A. Fedrizzi, Optica **5**, 514 (2018).
- [15] A. Pickston, F. Graffitti, P. Barrow, C. L. Morrison, J. Ho, A. M. Brańczyk, and A. Fedrizzi, Optics Express **29**, 6991 (2021).
- [16] O. Gazzano, S. Michaelis de Vasconcellos, C. Arnold, A. Nowak, E. Galopin, I. Sagnes, L. Lanco, A. Lemaître, and P. Senellart, Nature Communications **4**, 1425 (2013).
- [17] N. Somaschi, V. Giesz, L. De Santis, J. C. Loredo, M. P. Almeida, G. Hornecker, S. L. Portalupi, T. Grange, C. Anton, J. Demory, C. Gomez, I. Sagnes, N. D. Lanzillotti-Kimura, A. Lemaître, A. Auffeves, A. G. White, L. Lanco, and P. Senellart, Nature Photonics **10**, 340 (2016).
- [18] F. Mann, H. M. Chrzanowski, M. Placke, F. Gewers, and S. Ramelow, Optica Quantum **3**, 495 (2025).
- [19] R. Ikuta, T. Kobayashi, H. Kato, S. Miki, T. Yamashita, H. Terai, M. Fujiwara, T. Yamamoto, M. Koashi, M. Sasaki, Z. Wang, and N. Imoto, Phys. Rev. A **88**, 042317 (2013).
- [20] S. Ates, I. Agha, A. Gulinatti, I. Rech, M. T. Rakher, A. Badolato, and K. Srinivasan, Phys. Rev. Lett. **109**, 147405 (2012).
- [21] J. H. Weber, B. Kambs, J. Kettler, S. Kern, J. Maisch, H. Vural, M. Jetter, S. L. Portalupi, C. Becher, and P. Michler, Nature Nanotechnology **14**, 23 (2019).
- [22] L. J. Wright, M. Karpiński, C. Söller, and B. J. Smith, Phys. Rev. Lett. **118**, 023601 (2017).
- [23] S. Kapoor, A. Rodek, M. Mikolajczyk, J. Szuniewicz, F. Sońnicki, T. Kazimierczuk, P. Kossacki, and M. Karpiński, Nanophotonics **14**, 1775 (2025).
- [24] J. Lavoie, J. M. Donohue, L. G. Wright, A. Fedrizzi, and K. J. Resch, Nature Photonics **7**, 363 (2013).
- [25] M. Allgaier, V. Ansari, L. Sansoni, C. Eigner, V. Quiring, R. Ricken, G. Harder, B. Brecht, and C. Silberhorn, Nature Communications **8**, 14288 (2017).
- [26] C. Joshi, B. M. Sparkes, A. Farsi, T. Gerrits, V. Verma, S. Ramelow, S. W. Nam, and A. L. Gaeta, Optica **9**, 364

---

- [1] E. Knill, R. Laflamme, and G. Milburn, Nature **409**, 46 (2001).
- [2] C.-Y. Lu, D. E. Browne, T. Yang, and J.-W. Pan, Phys. Rev. Lett. **99**, 250504 (2007).
- [3] B. P. Lanyon, T. J. Weinhold, N. K. Langford, M. Barbieri, D. F. V. James, A. Gilchrist, and A. G. White, Phys.

(2022).

[27] M. Karpiński, M. Jachura, L. J. Wright, and B. J. Smith, *Nature Photonics* **11**, 53 (2017).

[28] F. Sośnicki, M. Mikołajczyk, A. Golestani, and M. Karpiński, *Nature Photonics* **17**, 761 (2023).

[29] S. Mittal, V. V. Orre, A. Restelli, R. Salem, E. A. Goldschmidt, and M. Hafezi, *Phys. Rev. A* **96**, 043807 (2017).

[30] D. Zhu, C. Chen, M. Yu, L. Shao, Y. Hu, C. Xin, M. Yeh, S. Ghosh, L. He, C. Reimer, *et al.*, *Light: Science & Applications* **11**, 327 (2022).

[31] M. A. Seidler, X. J. Yeo, A. Cerè, and C. Kurtsiefer, *Phys. Rev. Lett.* **125**, 183603 (2020).

[32] L. Fan, C.-L. Zou, M. Poot, R. Cheng, X. Guo, X. Han, and H. X. Tang, *Nature Photonics* **10**, 766 (2016).

[33] S. Srivastava, D. B. Horoshko, and M. I. Kolobov, *Phys. Rev. A* **107**, 033705 (2023).

[34] S. Srivastava, D. B. Horoshko, and M. I. Kolobov, *Optics Express* **31**, 38560 (2023).

[35] M. Mazelanik, A. Leszczyński, and M. Parniak, *Nature Communications* **13**, 691 (2022).

[36] C. Joshi, B. M. Sparkes, A. Farsi, T. Gerrits, V. Verma, S. Ramelow, S. W. Nam, and A. L. Gaeta, *Optica* **9**, 364 (2022).

[37] L. Fan, C.-L. Zou, N. Zhu, and H. X. Tang, *Nature Photonics* **13**, 323 (2019).

[38] K. V. Mylswamy and A. M. Weiner, *Optics Letters* **45**, 5688 (2020).

[39] N. Couture, F. Bouchard, A. Sit, G. Thekkadath, D. England, P. J. Bustard, and B. J. Sussman, *Phys. Rev. Lett.* **135**, 153602 (2025).

[40] C. K. Hong, Z. Y. Ou, and L. Mandel, *Phys. Rev. Lett.* **59**, 2044 (1987).

[41] V. Torres-Company, J. Lancis, and P. Andres, *Progress in Optics* **56**, 1 (2011).

[42] F. Sośnicki, M. Mikołajczyk, A. Golestani, and M. Karpiński, *Applied Physics Letters* **116**, 234003 (2020).

[43] S. Kapoor, F. Sośnicki, and M. Karpiński, *APL Photonics* **10** (2025).

[44] B. H. Kolner, *Applied Physics Letters* **52**, 1122 (1988).

[45] W. Grice, R. Erdmann, I. Walmsley, and D. Branning, *Phys. Rev. A* **57**, 2289 (1998).

[46] M. Avenhaus, A. Eckstein, P. J. Mosley, and C. Silberhorn, *Optics Letters* **34**, 2873 (2009).

[47] K. Goda and B. Jalali, *Nature Photonics* **7**, 102 (2013).

[48] Y.-S. Kim, O. Slattery, P. S. Kuo, and X. Tang, *Phys. Rev. A* **87**, 063843 (2013).

[49] M. Pont, R. Albiero, S. E. Thomas, N. Spagnolo, F. Cecarelli, G. Corrielli, A. Brieussel, N. Somaschi, H. Huet, A. Harouri, A. Lemaître, I. Sagnes, N. Belabas, F. Sciarino, R. Osellame, P. Senellart, and A. Crespi, *Phys. Rev. X* **12**, 031033 (2022).

[50] F. Sośnicki and M. Karpiński, *Optics Express* **26**, 31307 (2018).

[51] D. Bouwmeester, J.-W. Pan, K. Mattle, M. Eibl, H. Weinfurter, and A. Zeilinger, *Nature* **390**, 575 (1997).

[52] X.-L. Wang, X.-D. Cai, Z.-E. Su, M.-C. Chen, D. Wu, L. Li, N.-L. Liu, C.-Y. Lu, and J.-W. Pan, *Nature* **518**, 516 (2015).

[53] A. He, X. Guo, K. Wang, Y. Zhang, and Y. Su, *Journal of Lightwave Technology* **38**, 4780 (2020).

[54] L. Ranno, P. Gupta, K. Grądkowski, R. Bernson, D. Weninger, S. Serna, A. M. Agarwal, L. C. Kimerling, J. Hu, and P. O'Brien, *ACS Photonics* **9**, 3467 (2022).

[55] D. Renaud, D. R. Assumpcao, G. Joe, A. Shams-Ansari, D. Zhu, Y. Hu, N. Sinclair, and M. Loncar, *Nature Communications* **14**, 1496 (2023).

[56] C.-W. Chou, J. Laurat, H. Deng, K. S. Choi, H. de Riedmatten, D. Felinto, and H. J. Kimble, *Science* **316**, 1316 (2007).

[57] Z.-D. Li, R. Zhang, X.-F. Yin, L.-Z. Liu, Y. Hu, Y.-Q. Fang, Y.-Y. Fei, X. Jiang, J. Zhang, L. Li, N.-L. Liu, F. Xu, Y.-A. Chen, and J.-W. Pan, *Nature Photonics* **13**, 644 (2019).

[58] M. Kauffman, W. Banyai, A. Godil, and D. Bloom, *Applied Physics Letters* **64**, 270 (1994).

[59] C. Drago and A. M. Brańczyk, *Canadian Journal of Physics* **102**, 411 (2024).

# Supplementary Material

## Quantum interference between spectral bandwidth mismatched photons

Jan Krzyżanowski,<sup>1</sup> Jerzy Szuniewicz,<sup>1</sup> Sanjay Kapoor,<sup>1</sup> Filip Sośnicki,<sup>1,2</sup> Michał Karpiński<sup>1</sup>

<sup>1</sup>Faculty of Physics, University of Warsaw, Pasteura 5, 02-093 Warszawa, Poland

<sup>2</sup>Integrated Quantum Optics, Institute for Photonic Quantum Systems (PhoQS),  
Paderborn University, Warburger Str. 100, D-33098, Paderborn, Germany

### Analytical model for ideal bandwidth converter

In this section, we analytically derive the fundamental upper limit on the Hong-Ou-Mandel (HOM) interference visibility using an ideal bandwidth conversion setup. We consider two independent photons in distinct spatial modes labeled by  $a$  and  $b$ .

$$|\psi_a\rangle = \int \phi_a(\omega) \hat{a}^\dagger(\omega) |\text{vac}\rangle, \quad (\text{S.1})$$

$$|\psi_b\rangle = \int \phi_b(\omega) \hat{a}^\dagger(\omega) |\text{vac}\rangle, \quad (\text{S.2})$$

where  $\hat{a}^\dagger(\omega)$  is the creation operator for a plane wave mode at frequency  $\omega$ .  $\phi_{a(b)}$  are the Gaussian spectral amplitude functions defined as:

$$\phi_a(\omega) = \frac{1}{(\pi\sigma_a^2)^{1/4}} \exp\left(-\frac{(\omega - \omega_0)^2}{2\sigma_a^2}\right), \quad (\text{S.3})$$

$$\phi_b(\omega) = \frac{1}{(\pi\sigma_b^2)^{1/4}} \exp\left(-\frac{(\omega - \omega_0)^2}{2\sigma_b^2}\right), \quad (\text{S.4})$$

where  $\sigma_a$  and  $\sigma_b$  are the spectral bandwidth parameters. We assume a spectral bandwidth mismatch where  $\sigma_a > \sigma_b$ . To match the bandwidth of photon  $a$  to photon  $b$ , we send the photon  $a$  through a bandwidth conversion setup. This setup consists of a dispersive element with group delay dispersion (GDD)  $\Phi$  followed by an ideal time lens (perfect quadratic temporal phase) with a chirp rate  $K = 1/\Phi$ .

The output spectral profile after bandwidth conversion can be determined using the time-to-frequency mapping proposed by Kauffman et al. [S1].

First, we determine the temporal profile of photon  $a$  via the Fourier transform of Eq. (S.3). For a transform-limited Gaussian pulse, the temporal width  $\sigma_{t,a}$  is inversely proportional to the spectral width  $\sigma_a$ . Specifically, the temporal envelope  $E_a(t)$  is proportional to:

$$E_a(t) \propto \exp\left(-\frac{t^2}{2(1/\sigma_a)^2}\right) = \exp\left(-\frac{t^2\sigma_a^2}{2}\right). \quad (\text{S.5})$$

The time-to-frequency mapping relates the output frequency axis  $(\omega - \omega_0)$  to the time axis  $t$  via the GDD parameter  $\Phi$ :

$$t = \Phi(\omega - \omega_0). \quad (\text{S.6})$$

Substituting this mapping into the temporal envelope gives the magnitude of the output spectral amplitude  $\phi'_a(\omega)$ :

$$|\phi'_a(\omega)| \propto E_a(t)|_{t=\Phi(\omega-\omega_0)} \propto \exp\left(-\frac{\Phi^2(\omega - \omega_0)^2\sigma_a^2}{2}\right). \quad (\text{S.7})$$

We can define the new output bandwidth  $\sigma'_a$  by inspecting the Gaussian exponent of the form  $\exp(-(\omega - \omega_0)^2/2\sigma'^2_a)$ :

$$\frac{1}{2\sigma'^2_a} = \frac{\Phi^2\sigma_a^2}{2} \implies \sigma'_a = \frac{1}{|\Phi|\sigma_a}. \quad (\text{S.8})$$

While the magnitude is transformed based on the input temporal shape, the time-lens setup imparts a residual quadratic spectral phase (chirp) [S1]. The full complex expression for the transformed waveform is:

$$\phi'_a(\omega) = \underbrace{\frac{1}{(\pi\sigma'^2_a)^{1/4}} \exp\left(-\frac{(\omega - \omega_0)^2}{2\sigma'^2_a}\right)}_{\text{magnitude}} \times \underbrace{\exp\left(i\frac{1}{2}\Phi(\omega - \omega_0)^2\right)}_{\text{residual quadratic phase}}. \quad (\text{S.9})$$

We seek to compress the bandwidth of photon  $a$  such that its output bandwidth matches photon  $b$ .

$$\sigma'_a = \sigma_b. \quad (\text{S.10})$$

Using Eq. (S.8), we obtain:

$$\frac{1}{|\Phi|\sigma_a} = \sigma_b. \quad (\text{S.11})$$

We can solve for the required GDD  $\Phi$ :

$$\Phi = \frac{1}{\sigma_a \sigma_b}. \quad (\text{S.12})$$

This implies that the necessary dispersion is the inverse product of the input and target bandwidths.

### Coincidence probability calculations

We now consider the interference of the transformed photon  $a$  and the original photon  $b$  at a 50 : 50 beam splitter.

1. **Mode  $a$  (transformed):** With  $\Phi = 1/(\sigma_a \sigma_b)$ , the spectral width is equal to  $\sigma_b$ .

$$\phi'_a(\omega) = \frac{1}{(\pi \sigma_b^2)^{1/4}} \exp\left(-\frac{(\omega - \omega_0)^2}{2\sigma_b^2}\right) \exp\left(i\frac{(\omega - \omega_0)^2}{2\sigma_a \sigma_b}\right). \quad (\text{S.13})$$

2. **Mode  $b$  (delayed):** Photon  $b$  passes through a delay line introducing a time delay  $\tau$ .

$$\phi_{b,\tau}(\omega) = \phi_b(\omega) e^{-i\omega\tau} = \frac{1}{(\pi \sigma_b^2)^{1/4}} \exp\left(-\frac{(\omega - \omega_0)^2}{2\sigma_b^2}\right) e^{-i\omega\tau}. \quad (\text{S.14})$$

The coincidence probability  $p(\tau)$  can be calculated using Eq. (17) from Drago et al. [S2],

$$p(\tau) = \frac{1}{2} - \frac{1}{2} \left| \int_{-\infty}^{\infty} d\omega \phi'_a(\omega) \phi_{b,\tau}^*(\omega) \right|^2. \quad (\text{S.15})$$

Substituting the specific functions and letting  $\Omega = \omega - \omega_0$ :

$$p(\tau) = \frac{1}{2} - \frac{1}{2} \frac{1}{\pi \sigma_b^2} \left| \int_{-\infty}^{\infty} d\Omega \exp\left(-\frac{\Omega^2}{\sigma_b^2}\right) \exp\left(i\frac{\Omega^2}{2\sigma_a \sigma_b}\right) \exp(i(\Omega + \omega_0)\tau) \right|^2. \quad (\text{S.16})$$

### Fundamental limit on the visibility due to the residual spectral phase

To find the best possible minimum coincidence probability (maximum visibility), we set the time delay  $\tau = 0$ . The integral in Eq. (S.16) becomes a Gaussian integral with a complex coefficient in the exponent.

Let the overlap integral be  $J$ :

$$J = \frac{1}{\sqrt{\pi \sigma_b}} \int_{-\infty}^{\infty} d\Omega \exp\left[-\Omega^2 \left(\frac{1}{\sigma_b^2} - i\frac{1}{2\sigma_a \sigma_b}\right)\right]. \quad (\text{S.17})$$

Using the standard Gaussian integral identity  $\int_{-\infty}^{\infty} e^{-Bx^2} dx = \sqrt{\frac{\pi}{B}}$ , with  $B = \frac{1}{\sigma_b^2} \left(1 - i\frac{\sigma_b}{2\sigma_a}\right)$ :

$$J = \frac{1}{\sqrt{\pi \sigma_b}} \sqrt{\frac{\pi}{B}} = \frac{1}{\sigma_b \sqrt{B}} = \frac{1}{\sqrt{1 - i\frac{\sigma_b}{2\sigma_a}}}. \quad (\text{S.18})$$

The term required for the coincidence probability is the squared modulus  $|J|^2$ :

$$|J|^2 = \frac{1}{\left|1 - i\frac{\sigma_b}{2\sigma_a}\right|} = \frac{1}{\sqrt{1 + \left(\frac{\sigma_b}{2\sigma_a}\right)^2}}. \quad (\text{S.19})$$

Substituting  $|J|^2$  back into the probability expression:

$$p_{\min} = \frac{1}{2} \left( 1 - \frac{1}{\sqrt{1 + \left( \frac{\sigma_b}{2\sigma_a} \right)^2}} \right). \quad (\text{S.20})$$

The maximum visibility of the interference can be calculated by the following expression:

$$V = \frac{p_{\max} - p_{\min}}{p_{\max} + p_{\min}} = \frac{F}{\sqrt{4F^2 + 1} - F}. \quad (\text{S.21})$$

where  $F = \sigma_a/\sigma_b$  is the spectral bandwidth compression factor. Equation S.21 indicates that for an increasing compression factor  $F$  (the residual phase variation in this regime becomes negligible over the target bandwidth), the visibility approaches 100% as shown in Fig. S1. For small values of  $F$ , the residual quadratic phase sets a fundamental limit on the visibility. For example, for 2-fold spectral compression,  $V = 94.2\%$  and quickly approaches 100% with increasing  $F$ , for 10-fold compression  $V = 99.75\%$ .

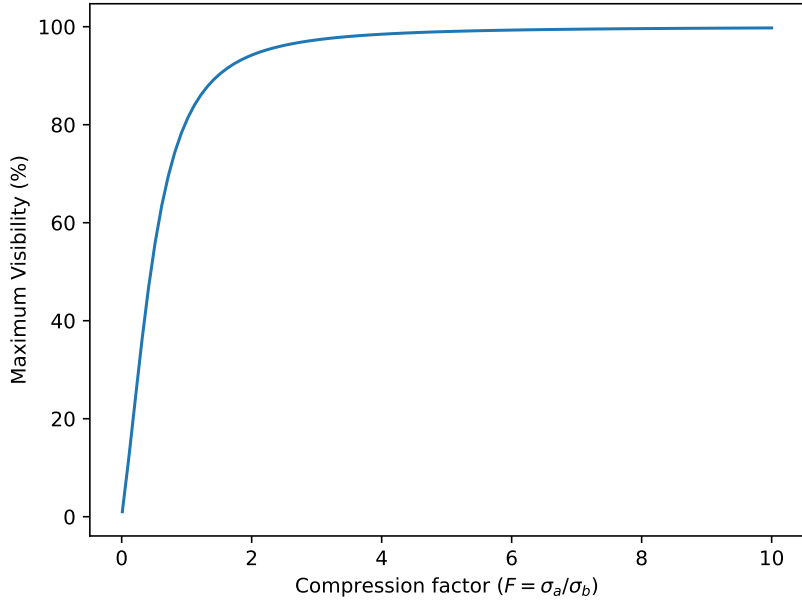


FIG. S1. Maximum visibility as a function of ratio of spectral bandwidth  $\sigma_a$  of target photon to the bandwidth ( $\sigma_b$ ) of input photon according to Eq. (S.21). As the compression factor increases, the maximum visibility approaches 100%.

#### Numerical simulations of the sinusoidal time lens

To model the experimental reality, we perform numerical simulations using a sinusoidal phase profile  $\theta(t) = -A \cos(2\pi f_m t)$  provided by the electro-optic phase modulator. Here  $f_m$  is the modulation frequency, and  $A$  is the phase modulation amplitude. This profile is an approximation of the ideal parabolic phase profile, leading to higher-order temporal aberrations that degrade the HOM visibility [S3]. We evaluate the bandwidth conversion performance across three distinct scenarios for a 10-fold spectral bandwidth compression of an input photon centered at 1550 nm with a 2.0 nm full-width at half-maximum (FWHM) bandwidth to a target of bandwidth 0.2 nm. The results are summarized in Table I.

### Numerical optimization for maximum visibility

This simulation serves to establish the highest possible HOM visibility achievable using a sinusoidal time lens, by performing a brute-force optimization of all system parameters: GDD ( $\Phi$ ), modulation frequency ( $f_m$ ), and modulation amplitude ( $A$ ). We found the optimal set of parameters to be  $f_m = 3.49$  GHz,  $A = 58.37\pi$  rad, and  $\Phi = 11.39$  ps $^2$ . This configuration results in a maximum theoretical visibility of  $V = 98.63\%$  as shown in Fig. S2 (a). The corresponding marginal spectral distribution of the converted photon, shown in Fig. S2 (b), is nearly perfectly Gaussian, demonstrating that near-perfect indistinguishability can, in principle, be restored if the required large modulation amplitude is achieved.

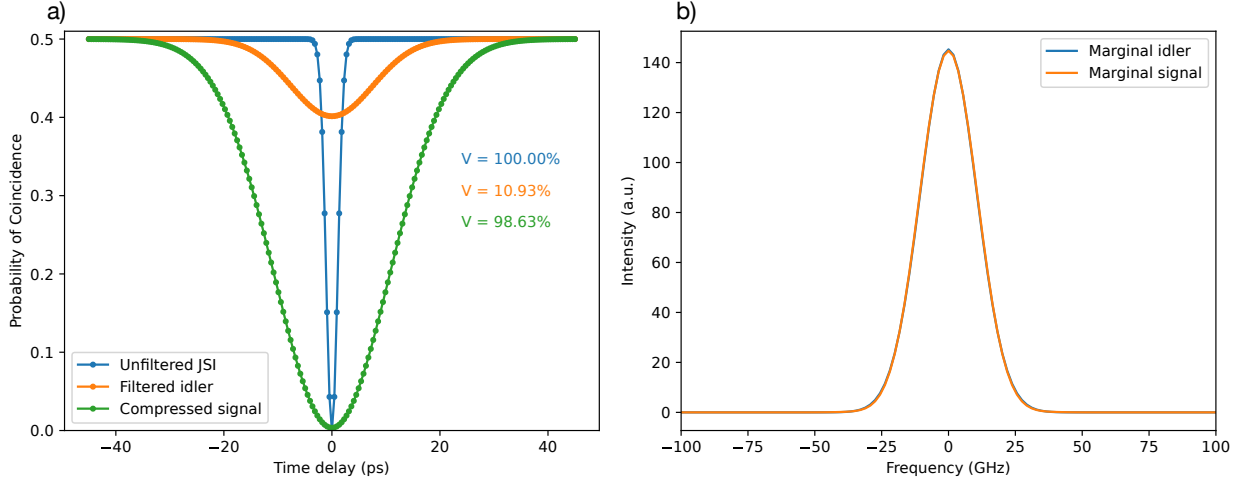


FIG. S2. Spectral bandwidth compression with numerically optimized parameters. (a) Simulated Hong-Ou-Mandel (HOM) interference for the initial biphoton state (blue), the state after filtering the idler (orange), and the state after signal compression using optimized sinusoidal time lens parameters (green). Brute-force optimization of the modulation frequency, amplitude, and GDD allows for the retrieval of near-perfect indistinguishability ( $V = 98.63\%$ ). (b) Marginal spectral distributions of the filtered idler and the compressed signal. Under these optimal parameters, the compressed signal closely matches the Gaussian profile of the target idler.

### Realistic modulation amplitude limit

This scenario addresses experimental feasibility by imposing a strict, physically realistic upper limit on the modulation amplitude  $A$ . We set the modulation amplitude to  $A = 12.57$  rad ( $4\pi$ ), which is easily achievable with our EOPMs, and optimized the other parameters, yielding  $f_m = 14.29$  GHz and  $\Phi = 11.29$  ps $^2$ . Operating under this amplitude constraint, the system is more susceptible to temporal aberrations [S3]. These aberrations cause distinct spectral side-lobes to appear in the marginal distribution as shown in Fig. S3 (b). These side-lobes introduce indistinguishability, lowering the maximum achievable visibility to  $V = 87.26\%$  as can be seen in Fig. S3 (a).

### Simulation of experimental configuration

Finally, we simulate the specific parameters used in the experimental setup described in the main text to validate our experimental results. We fix the GDD provided by the (1-km-long SMF-28) fiber spool at  $\Phi = 22$  ps $^2$ , the modulation frequency at  $f_m = 10$  GHz, and optimize for the modulation amplitude as done in the experiment resulting in a value of  $A = 4.27\pi$  rad. The simulation results in a visibility of  $V = 63.78\%$ . The marginal distribution for this case (Fig. S4 (b)) shows the most pronounced spectral side-lobes. This simulated visibility is in close agreement with our experimental result of  $(63.2 \pm 1.9)\%$ , confirming that the observed visibility drop is primarily attributed to non-optimal dispersion used in the experiment due to limited options for the dispersion compensation modules available in the lab to achieve non-dispersive delay of the signal photon.

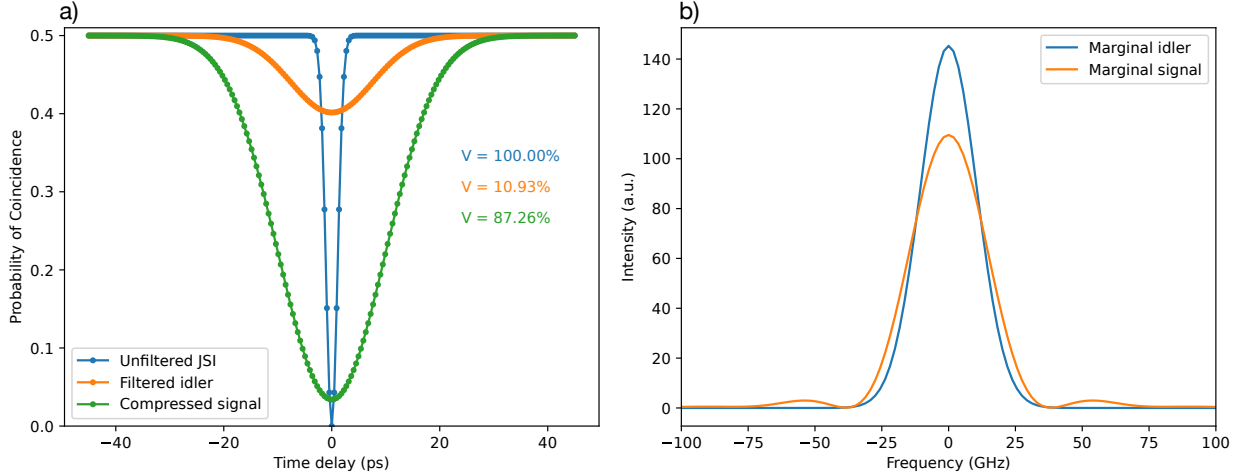


FIG. S3. Impact of realistic modulation amplitude constraints on HOM visibility. (a) HOM interference simulated with a practical upper limit on the modulation amplitude  $A = 4\pi$ . The restriction on phase modulation amplitude limits the achievable visibility to 87.27%, demonstrating the impact of temporal aberrations. (b) The marginal distribution of the compressed signal photon shows the emergence of spectral side-lobes. These features are a direct result of higher-order temporal aberrations introduced by the sinusoidal phase profile when operating away from the numerically optimal parameters.

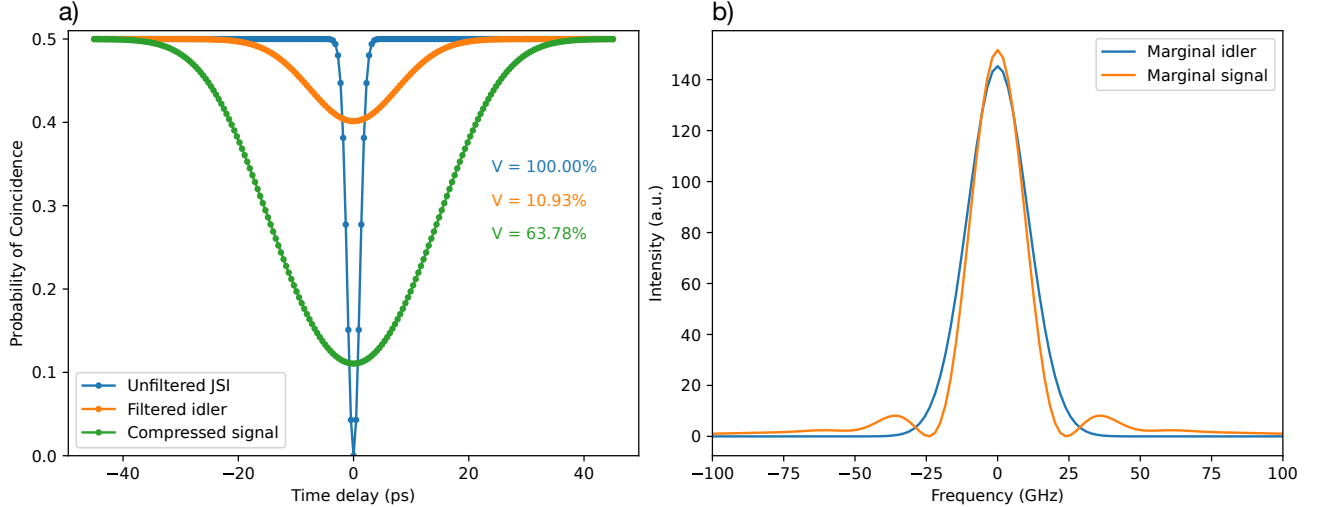


FIG. S4. Simulation of the laboratory experimental configuration. (a) HOM interference simulated using the exact parameters employed in the main text ( $\Phi = 22 \text{ ps}^2$ ,  $f_m = 10 \text{ GHz}$ ,  $A = 13.44 \text{ rad}$ ). The resulting visibility of 63.78% is in close agreement with the experimental measurement of  $(63.2 \pm 1.9)\%$ , validating the numerical model. (b) Marginal spectral distributions showing prominent side-lobes in the signal photon.

### Experimental details and data

In Fig. S5, we provide plots of directly measured coincidence count rates for HOM interference without any normalization. In Fig. S5(a) we show the data used to produce in Fig. 4 in the main text but without normalization.

For the measurements with unmodified signal photon we removed the bandwidth converter and the reference photon's fiber delay from the setup to avoid introducing additional distinguishability with dispersive elements, as discussed in the main text. This modification required an additional calibration of the delay axis. We perform the calibration by observing the HOM dip after disabling the filter that was used to create the narrowband photon. We disable the filter by displaying the appropriate phase pattern in the pulse shaper.

We present the dip without the filter (in green) in Fig. S5(b) together with the dip measured with the filter and without the bandwidth converter (in red, the same as in Fig. S5(a)). Both dips in this figure were measured at the same position of the delay line. Observation of the dip with the disabled filter at the same delay as with the enabled filter and without the bandwidth converter (Fig. S5 (b)) confirms the proper calibration of the delay axis in Fig. 4.

TABLE I. Comparison of simulated maximum visibility cases for sinusoidal time lens

Case	Description	$f_m$ (GHz)	$A$ ( $\pi$ rad)	GDD (ps $^2$ )	Visibility
1	Numerical optimization	3.49	58.4	11.39	98.63%
2	Realistic amplitude limit	14.29	4.0	11.29	87.26%
3	Experimental configuration	10.00	4.3	22.00	63.78%

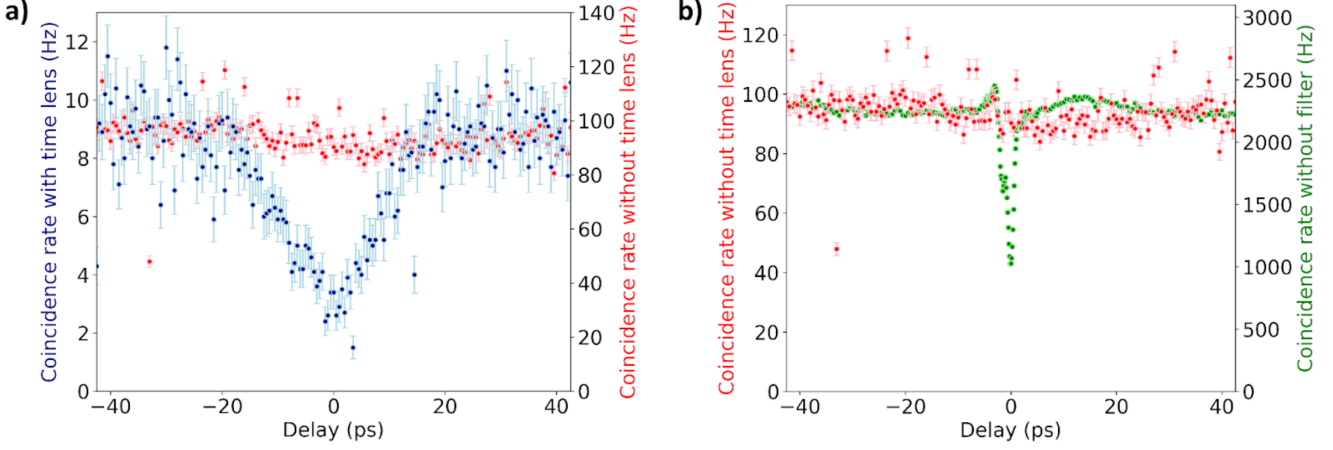


FIG. S5. Hong-Ou-Mandel dips without normalization. In a) we present the coincidence rates with (in blue) and without (in red) the bandwidth converter (raw experimental data for Figure 4 in the main text). The zero delay at the horizontal axis is provided with the same procedure as for Fig. 4 in the main text. As shown there is no visible dip without the converter and a clearly visible one with the converter, similarly to Fig. 4. In b) we show the same dip without the bandwidth converter as in a) (in red) and the dip observed after removing the filter from the setup (in green). We measured the dips in b) at the same positions at the delay line in both cases. We set the zero delay to be at the position of the green dip. As shown the clearly visible HOM dip appears after filter removal, which is a confirmation that the delay line was at the right position to observe the HOM interference for highly mismatched photons (red data, with spectral filter and without bandwidth converter). Error bars assume Poisson photon count statistics.

[S1] M. Kauffman, W. Banyai, A. Godil, and D. Bloom, *Applied Physics Letters* 64, 270 (1994).

[S2] C. Drago and A. M. Brańczyk, *Canadian Journal of Physics* 102, 411 (2024).

[S3] S. Kapoor, F. Sońnicki, and M. Karpiński, *APL Photonics* 10 (2025).